Twisted Tetrathiafulvalene Crystals

Journal:	*Molecular Systems Design & Engineering*
Manuscript ID	ME-ART-01-2022-000010.R1
Article Type:	Paper
Date Submitted by the Author:	15-Feb-2022

Complete List of Authors:	Yang, Yongfan; New York University, Chemistry Zong, Kai; Stevens Institute of Technology, Chemical Engineering and Materials Science Whittaker, St. John; New York University, Chemistry An, Zhihua; New York University, Chemistry Tan, Melissa; New York University, Chemistry Zhou, Hengyu; New York University, Department of Chemistry Shtukenberg, Alexander; New York University, Department of Chemistry Kahr, Bart; New York University, Department Chemistry and Molecular Design Institute Lee, Stephanie; New York University, Department of Chemistry and Molecular Design Institute; Stevens Institute of Technology, Department of Chemical, Biomedical and Material Engineering

ARTICLE

Twisted Tetrathiafulvalene Crystals

Yongfan Yang,[a] Kai Zong,[b] St. John Whittaker,[a] Zhihua An,[a] Melissa Tan,[a] Hengyu Zhou,[a] Alexander G. Shtukenberg,[a*] Bart Kahr,[a*] Stephanie S. Lee[a,b*]

Received 00th January 20xx,
Accepted 00th January 20xx

DOI: 10.1039/x0xx00000x

Optically-active optoelectronic materials are of great interest for many applications, including chiral sensing and circularly polarized light emission. Traditionally, such applications have been enabled by synthetic strategies to design chiral organic semiconductors and conductors. Here, centrosymmetric tetrathiafulvalene (TTF) crystals are rendered chiral on the mesoscale by crystal twisting. During crystallization from the melt, helicoidal TTF fibers were observed to grow radially outwards from a nucleation centre as spherulites, twisting in concert about the growth direction. Because molecular crystals exhibit orientation-dependent refractive indices, periodic concentric bands associated with continually rotating crystal orientations were observed within the spherulites when imaged between cross polarizers. Under certain conditions, concomitant crystal twisting and bending was observed, resulting in anomolous crystal optical behavior. X-ray diffraction measurements collected on different spherulite bands indicated no difference in the molecular packing between straight and twisted TTF crystals, as expected for microscopic twisting pitches between 20 – 200 μm. Mueller Matrix imaging, however, revealed preferential absorption and refraction of left- or right-circularly polarized light in twisted crystals depending on the twist sense, either clockwise or counterclockwise, about the growth direction. Furthermore, hole mobilities of $2.0 \pm 0.9 \times 10^{-6}$ cm^2/V-s and $1.9 \pm 0.8 \times 10^{-5}$ cm^2/V-s were measured for straight and twisted TTF crystals deposited on organic field-effect transistor platforms, respectively, demonstrating that crystal twisting does not negatively impact charge transport in these systems.

Design, System, Application

Small-molecule organic semiconductors are actively explored for optoelectronic applications, including solar panels, active matrix displays, and photodetectors. For systems incorporating chiral components, additional functions related to, for example, chiral light detection and emission become attainable. In this study, we induce spontaneous twisting of centrosymmetric tetrathiafulvalene (TTF) crystals upon crystallization from the melt in the presence of 10-15 wt% Canada balsam or one of its major components, abietic acid. During spherulitic growth, crystals twist in concert with either a right-handed or left-handed twisting sense, introducing chirality to the TTF film. Crystal twisting renders the TTF film optically active, preferentially interacting with left- or right-circularly polarized light depending on the twisting direction. Hole mobilities measured using organic field-effect transistor platforms are slightly improved for devices comprising twisted crystals compared to straight crystals, indicating crystal twisting as a simple and effective strategy to introduce optical activity to films comprising achiral organic semiconductors while retaining electronic performance.

1. Introduction

Tetrathiafulvalene (TTF) has been a workhorse – and a show horse – for the organic electronics community ever since its discovery in the 1970s. Over the past five decades, more than fifteen thousand papers have been published on the synthesis and characterization of TTF, TTF-based charge transfer complexes (CTCs), and TTF derivatives.[1, 2] It has been a laboratory for charge and charge transport.[2-4] The first demonstration of a metallic charge transfer complex, for example, was based on co-crystals of TTF and tetracyano-*p*-quinodimethane (TCNQ).[5-8] Since then, thousands of TTF analogues have been synthesized for optoelectronic applications, including transistors,[9] solar cells,[10, 11] and light-emitting diodes.[12, 13]

Of the enormous body of literature on TTF, most are dedicated to derivatizing the conjugated heterocyclic base structure, enhancing electrical conductivity or introducing structures that provide a chemical handle for other uses—such as 18-crown-6 fused TTF designed for chemical sensing.[14] In recent years, interest has grown

a. Molecular Design Institute, Department of Chemistry, New York University, New York, NY, USA.
Email: shtukenberg@mail.ru; bart.kahr@nyu.edu; stephlee@nyu.edu
b. Department of Chemical Engineering and Materials Science, Stevens Institute of Technology, Hoboken, NJ, USA.

in developing optically active TTF structures for applications in chiral sensors,[15] circularly polarized light emission[16] and switchable chiro-optical materials.[17, 18] All three oxidation states of TTF, TTF^0 with C_{2v} symmetry and TTF^{1+} and TTF^{2+} with D_{2h} symmetry are achiral and optically inactive in solution. In 2000, a binaphthylic TTF derivative was synthesized in which the molecule retained redox variability while displaying natural optical activity in solution.[19] Later on, optical active TTFs sported chiral sidechains,[20] cyclophane architectures,[21] and spiro-bisindene cores[22] while preserving electronic properties.

In the above examples, chirality was induced through the desymmetrization of the TTF molecule. Here, we grow TTF crystals in such a way that they adopt helicoidal morphologies. Dissymmetric ensembles of twisted crystals express a differential interaction with left and right circular polarization states by virtue of a precession of the refractivity along the light path. In this way, they resemble cholesteric liquid crystals with misaligned anisotropic layers. While well-established in the liquid crystal field, twisting in molecular compounds is a little-known, albeit common, phenomenon.[23] During spherulitic growth of crystals from the melt, individual crystal fibres grow radially outwards from the spherulite nucleation centre. Under some conditions, for example in the presence of a small molecule or polymer additive, these fibres spontaneously twist in unison, giving optical texture to films by virtue of synchronous rhythmic reorientations. Concentric bands of constant refractivity emerge with spacings (half-pitches) on the sub-micron to hundreds of microns length scale. Helicoids are chiral and can be right-handed or left-handed. Circular extinction and retardance both depend on the twist sense. Crystal twisting thus decouples chirality from molecular structure.

We have discovered that TTF can form banded spherulites of twisted crystals when crystallized from the melt in the presence of 10 – 15 wt% Canada balsam or one of its most abundant resin acids, abietic acid. These additives increase melt viscosity and favour the formation of thinner fibres, which have the effect of inducing crystal twisting in a number of systems.[24] No measurable change in the local packing arrangement of twisted TTF crystals compared to straight TTF crystals was detected by powder X-ray diffraction (PXRD), as expected for twisting pitches on the micron length scale. Still, wholly new properties of circular extinction and retardance were observed due to the dissymmetric nature of twisting. The hole mobilities of these melt-processed TTF films was also measured in organic field-effect transistors (OFETs), with a modest improvement in charge mobility observed for OFETs with active layers comprising twisted TTF crystals compared to those comprising straight TTF crystals.

2. Experimental Methods

TTF film fabrication. TTF (1–2 mg) powder (Sigma 99%, T_m = 115 °C) was mixed with either 10 – 15 wt% abietic acid or Canada balsam. The mixture was then melted between a glass slide and a cover slip at 120 °C. The sample was then immediately placed on an aluminum block maintained at the specified undercooling temperature, T_c to be crystallized at high supercooling. Complete crystallization occurred within 4 – 5 s.

Powder X-ray diffraction. X-ray microdiffraction (μ-XRD) was performed using a Bruker D8 Discover General Area Detector Diffraction System (GADDS) equipped with a VÅNTEC-2000 two-dimensional (2D) detector and a sealed Cu-Kα source (λ = 1.54178 Å). The X-ray beam was monochromated with a graphite crystal and collimated with a 0.5 mm capillary collimator (MONOCAP). Films were loaded on a silicon chip for data acquisition and the sample-to-detector distance was 150 mm. To collect 1D powder patterns, TTF films were scraped from the glass supports and the powders were loaded into Kapton capillary tubes.

Mueller matrix microscopy. Optical properties were established with a Mueller matrix microscope using a monochromated white light LED source. An inverted light microscope (Zeiss), customized with dual rotating wave plates as polarization modulators (Scheme 1), was used to simultaneously map the linear and circular anisotropies of polycrystalline TTF films.[25, 26] These properties are encoded in the 16-element polarization transfer or Mueller matrix, M, that relates input polarization states to output states.[27] If the light intensity is captured by camera, M is composed of 16 images (Scheme 1b). The rotating wave plates produce a time-

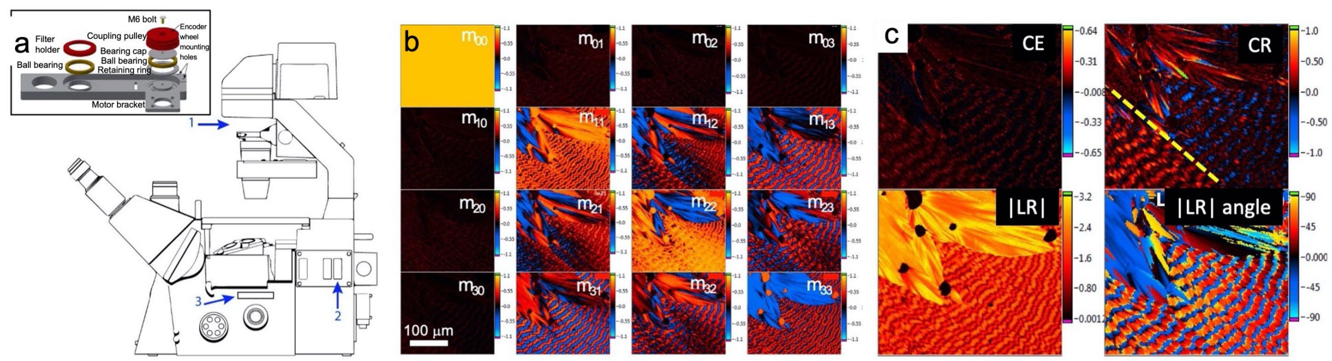

Scheme 1. (a) Schematic of Zeiss microscope. Numbered blue arrows show locations of 3D printed transmission (1), reflection (2), and detection (3) rotating wave plate polarization state modulators (inset). This data is collected in transmission from (1) → (3). (b) Mueller matrix of TTF banded spherulites measured at 500 nm. (c) Reduced properties of the differential Mueller matrix including circular extinction (CE), circular retardance (CR), the absolute value of the linear birefringence |LR| (in radians), and the angle of the larger refractive index measured clockwise from the horizon (in degrees). The CR subpanel in (c) indicates both right and left-handed twisting on either side of the broken yellow line, consistent with the centric symmetry of TTF crystals. Vertical scale in radians. Scale bar = 100 μm.

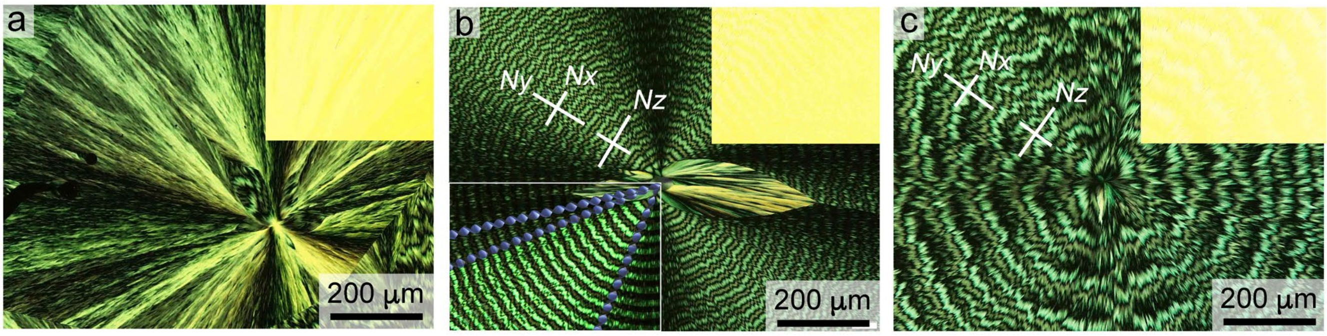

Figure 1. Optical micrographs of TTF films with 10 wt % abietic acid between crossed polarizers crystallized at (a) 50 °C, (b) 25 °C with P = 25 mm and (c) 25 °C with P = 100 mm. Overlayed purple helicoids in b illustrate relationship between crystal twisting and optical bands observed in cross polarized images. For reference, insets display overlayed linearly polarized optical images of the films in which very little contrast is visible.

dependent intensity signal at the detector that is subsequently demodulated to recover M, a convolution of contributions from several optical effects; consequently, the 'basis' quantities (eq. 1) must be recovered in the form of a differential matrix **L** propagated over some distance.[28, 29]

$$\mathbf{L} = \begin{bmatrix} -\mathrm{A} & -\mathrm{LE} & -\mathrm{LE}' & \mathrm{CE} \\ \mathrm{LE} & -\mathrm{A} & \mathrm{CR} & \mathrm{LR}' \\ \mathrm{LE}' & -\mathrm{CR} & -\mathrm{A} & -\mathrm{LR} \\ \mathrm{CE} & -\mathrm{LR}' & \mathrm{LR} & -\mathrm{A} \end{bmatrix} \approx \begin{bmatrix} m_{11} & m_{12} & m_{13} & m_{14} \\ m_{21} & m_{22} & m_{23} & m_{24} \\ m_{31} & m_{32} & m_{33} & m_{34} \\ m_{41} & m_{42} & m_{43} & m_{44} \end{bmatrix} \quad \text{(eq. 1)}$$

LE and LE' are the differential extinctions of linearly polarized light along the 0° and 90° azimuthal directions and the −45° and 45° directions, respectively. LR and LR' are the linear retardances for the same sets of axes (Scheme 1c). Elements along the anti-diagonal represent circular retardance, CR, and circular extinction, CE, (Scheme 1c)[30, 31] while elements along the capture the isotropic absorption, A.

LR and CR are given as the following:

$$\mathrm{LR} = 2\pi(n_{0°} - n_{90°})L/\lambda \quad \text{(eq. 2)}$$

and

$$\mathrm{CR} = 2\pi(n_L - n_R)L/\lambda \quad \text{(eq. 3)}$$

where $n_{0°}$ and $n_{90°}$ are the refractive indices for orthogonal polarizations, and n_L and n_R are refractive indices for left and right circularly polarized light. λ is wavelength of light. L is the crystal thickness.

Organic field-effect transistors (OFETs). OFET platforms were fabricated by evaporating 2 nm Cr/50 nm Au electrodes through a shadow mask onto 300 nm SiO_2/doped Si wafers. Straight and twisted TTF films were fabricated as described above, replacing the bottom glass slide with the OFET platform. For OFET measurements, the top coverslip was removed to access the electrodes.

3. Results and Discussion

Straight and twisted TTF crystal growth. TTF films were formed from the melt (T_m = 115 °C) sandwiched between a glass slide and a cover slip. At crystallization temperatures, T_c > 30 °C, TTF forms spherulites comprising straight crystals. Figure 1a displays images of a TTF film crystallized at around 50 °C in the presence of 10 wt% abietic acid. TTF crystallizes as yellow spherulites without significant contrast in linearly polarized light. Spherulite diameters ranged from hundreds of microns to millimeters (Figure 1a inset). Between crossed polarizers, crystalline fibrils growing radially outwards from the spherulite centre are apparent. A characteristic Maltese cross is also observed, with light extinction occurring when the growth direction is either parallel or perpendicular to one of the polarizers. Such morphology is typical of small molecule films crystallized from the melt and has been observed in a wide range of compounds.[23]

At crystallization temperatures < 30 °C, TTF films with 10 wt% abietic acid still crystallized as spherulites but with the presence of rhythmic concentric bands. The inset in Figure 1b displays a brightfield image of a banded yellow TTF spherulite crystallized at T = 25 °C. In this case, alternating lighter and darker bands are present, albeit faintly, in the linearly polarized image (Figure 1b inset). Between cross polarizers, the presence of sharply contrasting concentric bands overlayed by a Maltese extinction cross is more obvious (Figure 1b). The bands follow a pattern of alternating wide light and dark green bands, separated by thin black bands. The pitch, P^l, defined by the distance between two equi-coloured bands, was 25 µm. Defining the growth direction as N_y, out-of-plane crystal orientations oscillate between N_x and N_z directions as they twist about N_y. Two leaf-like domains are also observed at the spherulite centre. These leaves comprise straight TTF crystals that grow more slowly than the surrounding banded domains and disappear at distances > 300 µm from the spherulite centre.

Banded spherulites such as those formed by TTF have been most commonly observed in polymer films, such as polyethylene.[32] Over the past decade, we have identified over 100 small-molecule compounds that also form banded spherulites when grown from the melt,[23] and it is estimated that one-third of molecular crystals can adopt this morphology.[33] In these systems, the appearance of concentric bands arises from continuous twisting of crystalline fibrils about the growth direction, with thinner fibrils having a stronger propensity to twist compared to thicker fibrils.[34] The orientation of these crystals thus rotates rhythmically as the spherulite grows

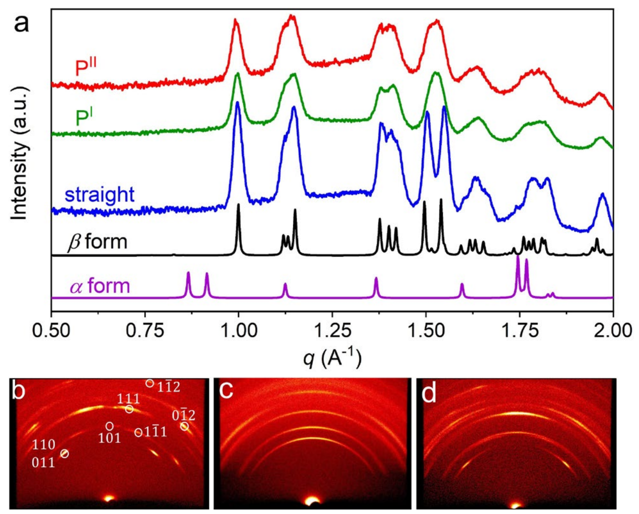

Figure 2. (a) Powder X-ray diffraction patterns for crystals loaded into Kapton capillary tubes. Simulated patterns were generated using Mercury (v3. 10. 1, 2018, Cambridge Crystallographic Database) based on single crystal structures in CCDC database (Reference codes: BDTOLE10 and BDTOLE02). (b-d) 2D X-ray diffraction patterns of TTF crystals (b) straight, (c) twisted crystals with small pitches, P^{I}, and (d) twisted crystals with large pitches, P^{II}, on the film.

radially outwards. Because these crystals exhibit orientation-dependent absorption and refraction of light, alternating "bands" appear in cross-polarized images corresponding to different orientations of the crystals with respect to the incident light. Illustrations of twisted fibrils are overlayed in Figure 1b.

A second banded morphology was observed to coexist in these films under the same growth conditions. Figure 1c shows this form in linearly polarized light (inset) and between crossed polarizers. This morphology, referred henceforth as P^{II}, is characterized by average pitches around 100 μm and the absence of the Maltese cross extinction characteristic of radial anisotropic bodies. As the anisotropy is undeniable, the condition of radial growth must be relaxed. Unlike P^{I} spherulites in Figure 1b, the boundaries between the bands are less well-defined. The jagged appearance of these boundaries indicates some disorder in the concerted twisting of fibrils as they grow radially outwards from the spherulite centre.

Crystal structure characterization. Figure 2a displays a comparison of TTF powders collected from scraping off films comprising straight crystals, P^{I}, and P^{II} spherulites. For reference, the simulated powder patterns of the commonly observed polymorphs of TTF, α and β,[35] are also provided. In all cases, the pattern matches that of the β phase. This phase has been found to form at higher temperatures, while the α phase is the thermodynamically stable phase at room temperature.[36] Furthermore, no measurable peak shifts among samples was detected. These results suggest that the crystal structure in these three morphologies observed in TTF melt-processed films are the same.

2D diffraction patterns were also collected to examine the orientation of TTF crystals in melt-processed films. As observed from strong texturing of the diffraction peaks in Figure 2b, TTF crystals in films comprising straight crystals adopt at least two preferred out-of-plane orientations. Peak assignments displayed in Figure 2b were made using indexGIXS, a Scilab-based software program that simulates 2D diffraction patterns for user-specified orientations.[37] In this case, we found most peaks in the diffraction pattern to be consistent with the β phase (101) plane parallel to the substrate surface.

Figure 2c and d display the 2D XRD patterns collected on P^{I} and P^{II} spherulites, respectively. The pattern on P^{I} spherulites exhibit a larger distribution of out-of-plane orientations, as expected for continuously twisting crystals with pitches of 25 μm. The diffraction pattern of P^{II} spherulites exhibit more texturing, albeit weaker than in the diffraction pattern of TTF spherulites comprising straight crystals. For both cases, peak locations are also consistent with the β phase of TTF.

Crystal twisting in P^{I} spherulites and twisting plus bending in P^{II} spherulites. While X-ray diffraction experiments confirm that all three morphologies adopt the same β polymorph, P^{I} and P^{II} spherulites exhibit different optical behaviour. P^{I} spherulites present concentric black arcs under crossed polarizers (Figure 3a), which correspond to zero birefringence. The birefringence of helical TTF fibres oscillates from $N_z - N_y$ to $N_y - N_x$, as displayed in Figure 1b. Between these two orientations there should be outcrops of optical axes where the birefringence is zero, leading to a black colour for all fibre orientations with respect to the crossed polarizers. These orientations are labeled as black lines in the helical single fibre illustrated in Figure 3b. When helical fibres assemble to form twisted spherulites, the black lines connect as black arcs because they twist in concert with one another (Figure 3c). Also, all bands are completely dark at 0° and 90° (Figure 3a), because light vibration directions in individual fibres are parallel to light vibration directions in the polarizer and analyser. The areas where such extinction occurs are shaded in grey in Figure 3c.

Compared with P^{I} spherulites, P^{II} spherulites exhibit similar zero birefringence arcs, but no complete extinction at 0° and 90°

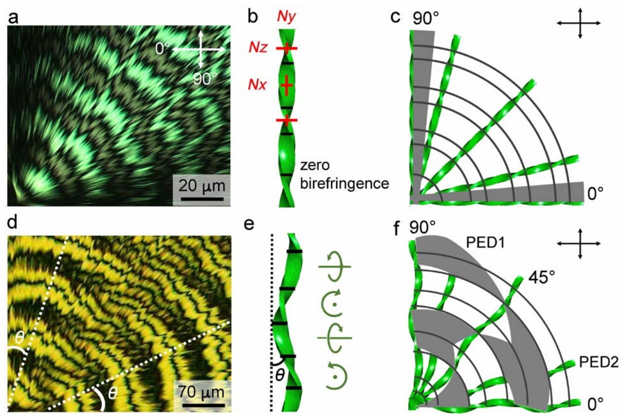

Figure 3. (a, d) One quarter of twisted TTF spherulite with (a) small and (d) large pitches under crossed polarizers. (b, e) Model for the structure of a fibre with only twisting and a combination of twisting and bending. (c, f) Illustration of assembled fibres in banded spherulites with (c) small and (f) large pitches. Zero birefringence bands are shown as black arcs, while areas of extinction are shaded in grey. Two partial extinction directions in (f) are labelled as PED1 and PED2. The orientation of crossed polarizers is illustrated in the top-right corner.

(Figure 3d). More dark bands appear at an angle of ~45° from the orientation of polarizers. Close to this orientation, the optical patterns of P^{I} and P^{II} spherulites are identical. As the spherulite is rotated between the polarizer and analyser, the pattern does not change, indicating that the spherulite maintains its radial symmetry and all fibres are the same along the azimuthal direction. To explain the unusual optical behaviour of P^{II} spherulites, we constructed a model in which TTF fibrils not only twist but also bend as they grow. Figure 3e illustrates this model. We assume that along the long axis of the fibre, the edge-on orientation at location 1 bends left, followed by the flat-on orientation bending into the plane at location 2. At location 3, the fibre bends right, and at location 4, it bends toward the viewing direction. We also assume that the regions with bending to the left or right dominate over regions with bending in and out of the plane because of insufficient space between the glass slides confining the film.

In Figure 3f, only main regions with bending to the left and right are considered to investigate the effect of bending on the optical properties. Fibres grow radially from a central nucleus radially. At 0° and 90°, neither of two main orientations of fibres is parallel to the polarizers resulting in no complete extinction in these two directions. Instead, they adopt an angle, θ, with respect to orientation of polarizers. At 45°, both orientations are far away from the vibration directions of polarizers and no extinction is observed. Similar to P^{I} spherulites, all zero birefringence bands are clearly visible at this orientation (Figure 3a,d). At specific directions with the angle of θ or 90° - θ, one of the orientations of fibres is parallel to the light vibration direction in crossed polarizers. This configuration results in extinction along directions PED1 and PED2 (labelled by white dashed lines in Figure 3d), with the extinction bands appearing once for 2π rotation of the fibre.

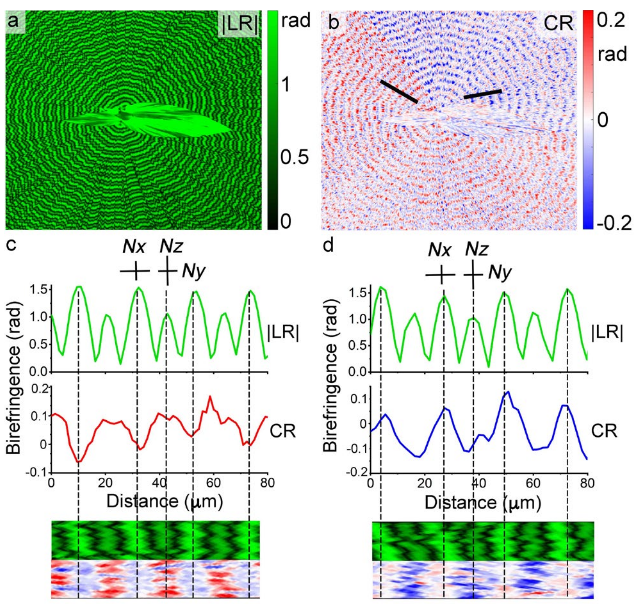

Figure 4. (a, b) Mueller Matrix images of a twisted spherulite with small pitches, PI, collected at λ= 550 nm: (a) linear retardance |LR| and (b) circular retardance (CR). (c,d) Signal intensities plotted along the paths (indicated by black lines on panel b) on the left and right sides, respectively.

Optical activity of banded TTF spherulites. While TTF itself is achiral, twisted crystals of TTF are chiral structures. Fibres must twist either clockwise or counterclockwise about the growth direction, breaking symmetry in the system. Films comprising twisted crystals thus present an opportunity to design optically active films independent of molecular structure. Organized systems built from misaligned optically anisotropic components[38-41] such as TTF can be productively analysed by Mueller matrix imaging (MMI).[42, 43]

To perform MMI, TTF films were placed between two continuously rotating retarders that modulate the polarization states of incoming and exiting light independently from one another. For every combination of incoming and exiting light polarization states, the light intensity at each pixel of the camera detector was collected. From this data, the optical properties of the film, namely linear and circular retardance and dichroism, can be extracted and mapped spatially (see Experimental Methods for more details). Figure 4 displays two MMI micrographs collected on a TTF P^{I} spherulite in the same region as that displayed in Figure 1b. Figure 4a represents the linear retardance signal extracted from MMI analysis. As observed in the image, the LR signal oscillates between small and large values in the radial direction from the spherulite centre. These bands correspond to those observed under cross polarized light and are the result of continuously rotating out-of-plane orientations of the twisted crystals about the growth direction. For banded TTF spherulites, the birefringence oscillates from $N_z - N_y$ = 0.044 (dark rings) to $N_y - N_x$ = 0.066 (bright rings), where N_y is the growth direction (Figure 1b).

Circular retardance (CR), that is, the refraction of circularly polarized light, was also extracted from MMI analysis. For an achiral material such as TTF, the CR is expected to be 0. Indeed, the CR signal collected on TTF spherulites comprising straight spherulites indicates no optical activity in these films. Figure 4b, on the other hand, displays a 2D map of the CR signal collected on the same banded TTF spherulite. As for the LR signal, periodic oscillations in the CR signal corresponding to the spherulite bands are observed. Furthermore, the CR micrograph reveals that the spherulite is bisected into two sections, one with a positive CR signal and one with a negative CR signal. The former corresponds to a (dextrorotatory) clockwise rotation of polarized light to the right when facing the oncoming radiation, while the latter corresponds to a levorotatory (counter clockwise) rotation of polarized light. The two fields are composed with twisted fibrils with opposing senses. Along spherulite radius, CR oscillates smoothly from almost zero to positive at the left half (Figure 4c) and to negative at the right half (Figure 4d), out of phase and in phase with |LR|, respectively.

Compared to synthetic routes to design chiral TTF derivatives, the generation of optical activity by twisting TTF crystals occurs spontaneously during crystallization from the melt. We have observed similar optical activity in other systems of twisted molecular crystals, including aspirin[44] and mannitol.[45] We have previously found that twisted crystals in banded spherulites form thin lamellae. These lamellae twist in concert with one other as they grow radially outwards from the spherulite centre. Due to space constraints, these lamellae splay as they twist, and the observed CR signal is a result of the misorientation of these stacked lamellae as they splay.[46]

Charge mobility. The introduction of twisting to semiconducting TTF also presents an opportunity to explore how crystal twisting affects optoelectronic properties. As a proof-of-concept, we fabricated organic field-effect transistors (OFETs) comprising straight crystals and twisted P^I TTF crystals. Curiously, P^{II} spherulites did not readily form on transistor platforms, perhaps related to differences in surface roughness between the glass substrates used for optical characterization and the SiO_2/-doped Si wafers used for transistors, and thus were not included in this comparison. Figure 5a displays an optical micrograph of an OFET channel in which a film comprising P^I TTF spherulites was deposited on top of gold source and drain electrodes. For all devices, the spherulitic growth direction was aligned parallel to the current flow direction. For a channel length of 100 um and a twisting pitch of 25 μm, approximately four full twists were present within the device channels. Figure 5b displays transfer curves collected in the saturation regime in which V_{SD} = -50 V and V_G was swept from 20 to -40 V in 1 V increments for TTF OFETs comprising straight and twisted crystals. OFETs comprising twisted TTF crystals display higher current flow than those comprising straight TTF crystals, corresponding to an order of magnitude improvement in the hole mobility, μ_h, from 2.0 $\pm$ 0.9 x10^{-6} cm^2/V^{-s} to 1.9 $\pm$ 0.8 x10^{-5} cm^2/V^{-s}, averaged over at least three devices for each type. This improvement of hole mobility for OFETS comprising twisted crystals is in line with our previous finding for twisted charge transfer complexes.[47]

The origin of this improvement in OFET mobility upon crystal twisting remains unknown. Crystal twisting pitches on the tens of microns length scale translate to a less than 0.01° rotation between adjacent molecular layers, so we do not expect twisting to significantly affect the charge transfer integral between adjacent molecules in crystals. We speculate that charge injection and extraction from the electrodes may be more efficient at specific out-of-plane crystal orientations present in twisted TTF crystals, which are absent in highly oriented straight TTF crystals. Film morphology also plays a significant role in determining overall charge transport in OFETs, and we are currently performing detailed microstructural analysis to understand the nature of grain boundaries and defects in these systems. Still, our results demonstrate that melt-processed TTF spherulites are electronically active and that crystal twisting provides modest improvements in charge mobility.

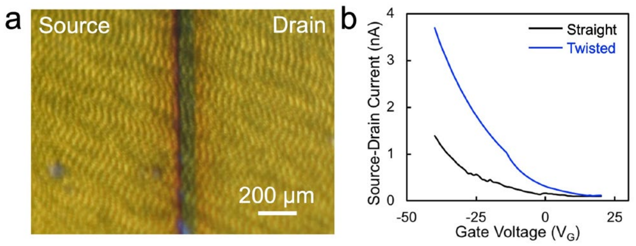

Figure 5. (a) Optical micrograph of an OFET channel comprising a film of TTF PI spherulites, with the gold source and drain electrodes labelled. (b) OFET transfer curves for active layers comprising spherulites of straight and twisted TTF crystals in which VSD = -50 V and VG was swept from 20 to -40 V.

4. Conclusions

By maintaining charge transport while introducing optical activity, spontaneous crystal twisting from the melt presents a means to impart novel materials properties to the already existing, enormous library of small-molecule organic semiconductors. Here, we demonstrate this concept with quintessential organic semiconductor TTF. Typically, TTF, a centrosymmetric molecule, forms centrosymmetric crystals that do not exhibit optical activity. When induced to form symmetry-broken twisted crystals, however, TTF preferentially interacts with left- or right-circularly polarized light depending on the crystal twisting sense. Optically active organic semiconducting systems are being explored for circularly polarized light detectors[48] and emitters.[49] Active materials for these systems are generally imparted chirality at the molecular level via synthetic routes.[50] Crystal twisting, on the other hand, can be applied to existing molecules irrespective of their molecular structure. Furthermore, melt processing to form organic semiconducting thin films eliminates the need for toxic organic solvents used for solution processing, the current dominant mode of film fabrication. Given the common occurrence of crystal twisting in at least a third of small-molecule systems we have examined over the past decade,[23] we expect crystal twisting to be a generalizable strategy in the organic electronics field with widespread implications.

Conflicts of interest

There are no conflicts to declare.

Acknowledgements

This work was primarily supported by the National Science Foundation DMR-2003968 and secondarily by the New York University Materials Research Science and Engineering Center (MRSEC) program of the National Science Foundation under award number DMR-1420073. The X-ray microdiffractometer with GADDS was acquired through the support of the National Science Foundation under Award Number CRIF/CHE-0840277 and NSF MRSEC Program under Award Number DMR-0820341. The authors also acknowledge support from PSEG to advance energy innovation at Stevens Institute of Technology. The authors thank Dr. Chunhua (Tony) Hu for assistance with X-ray diffraction experiments, Dr. Detlef.-M. Smilgies for assistance with indexGIXS, and Dr. Camille Farfan for graphic design support.

References

1. M. Bendikov, F. Wudl and D. F. Perepichka, *Chemical Reviews*, 2004, **104**, 4891-4946.
2. N. Martín, *Chemical Communications*, 2013, **49**, 7025.

3. R. Pou-Amérigo, E. Ortí, M. Merchán, M. Rubio and P. M. Viruela, *The Journal of Physical Chemistry A*, 2002, **106**, 631-640.
4. P. W. Thulstrup, S. V. Hoffmann, N. C. Jones and J. Spanget-Larsen, *Chemical Physics Impact*, 2021, **2**, 100009.
5. J. Ferraris, D. O. Cowan, V. Walatka and J. H. Perlstein, *Journal of the American Chemical Society*, 1973, **95**, 948-949.
6. H. Alves, A. S. Molinari, H. Xie and A. F. Morpurgo, *Nature Materials*, 2008, **7**, 574-580.
7. J. R. Kirtley and J. Mannhart, *Nature Materials*, 2008, **7**, 520-521.
8. J. Xiao, Z. Yin, H. Li, Q. Zhang, F. Boey, H. Zhang and Q. Zhang, *Journal of the American Chemical Society*, 2010, **132**, 6926-6928.
9. M. Mas-Torrent and C. Rovira, *Journal of Materials Chemistry*, 2006, **16**, 433-436.
10. N. Martín, L. Sánchez, M. Á. Herranz, B. Illescas and D. M. Guldi, *Accounts of Chemical Research*, 2007, **40**, 1015-1024.
11. N. Duvva, U. Chilakamarthi and L. Giribabu, *Sustainable Energy & Fuels*, 2017, **1**, 678-688.
12. A. Nollau, M. Pfeiffer, T. Fritz and K. Leo, *Journal of Applied Physics*, 2000, **87**, 4340-4343.
13. F. Pointillart, B. Le Guennic, O. Cador, O. Maury and L. Ouahab, *Accounts of Chemical Research*, 2015, **48**, 2834-2842.
14. J. L. Segura and N. Martín, *Angewandte Chemie International Edition*, 2001, **40**, 1372-1409.
15. Y. Zhou, D. Zhang, L. Zhu, Z. Shuai and D. Zhu, *The Journal of Organic Chemistry*, 2006, **71**, 2123-2130.
16. B. Lefeuvre, C. A. Mattei, J. F. Gonzalez, F. Gendron, V. Dorcet, F. Riobé, C. Lalli, B. Le Guennic, O. Cador, O. Maury, S. Guy, A. Bensalah-Ledoux, B. Baguenard and F. Pointillart, *Chemistry – A European Journal*, 2021, **27**, 7362-7366.
17. M. Gaedke, F. Witte, J. Anhäuser, H. Hupatz, H. V. Schröder, A. Valkonen, K. Rissanen, A. Lützen, B. Paulus and C. A. Schalley, *Chemical Science*, 2019, **10**, 10003-10009.
18. E. Cariati, X. Liu, Y. Geng, A. Forni, E. Lucenti, S. Righetto, S. Decurtins and S. X. Liu, *Physical Chemistry Chemical Physics*, 2017, **19**, 22573-22579.
19. R. Gómez, J. L. Segura and N. Martín, *Organic Letters*, 2000, **2**, 1585-1587.
20. E. Gomar-Nadal, C. Rovira and D. B. Amabilino, *Tetrahedron*, 2006, **62**, 3370-3379.
21. K. Kobayakawa, M. Hasegawa, H. Sasaki, J. Endo, H. Matsuzawa, K. Sako, J. Yoshida and Y. Mazaki, *Chemistry - An Asian Journal*, 2014, **9**, 2751-2754.
22. M. Hasegawa, D. Kurebayashi, H. Matsuzawa and Y. Mazaki, *Chemistry Letters*, 2018, **47**, 989-992.
23. A. G. Shtukenberg, X. Zhu, Y. Yang and B. Kahr, *Crystal Growth & Design*, 2020, **20**, 6186-6197.
24. E. Cariati, X. Liu, Y. Geng, A. Forni, E. Lucenti, S. Righetto, S. Decurtins and S. X. Liu, *Phys Chem Chem Phys*, 2017, **19**, 22573-22579.
25. M. Tan, Ph.D. Thesis. New York University, 2020.
26. S. M. Nichols, Ph.D. Thesis. New York University, 2018.
27. R. A. Chipman, W.-S. T. Lam and G. Young, *Polarized light and optical systems*, CRC Press, 2018.
28. R. M. A. Azzam and N. M. Bashara, *Ellipsometry and Polarised Light*, North-Holland, Amsterdam, 1988.
29. O. Arteaga and A. Canillas, *Opt. Lett.*, 2010, **35**, 559-561.
30. A. T. Martin, S. M. Nichols, V. L. Murphy and B. Kahr, *Chemical Communications*, 2021, **57**, 8107-8120.
31. O. Arteaga and B. Kahr, *JOSA B*, 2019, **36**, F72-F83.
32. H. D. Keith and F. J. Padden, *Macromolecules*, 1996, **29**, 7776-7786.
33. F. Bernauer, *Gedrillte Kristalle: Verbreitung, Entstehungsweise und Beziehungen zu optischer Aktivit \ a t und Molek \ u lasymmetrie*, Gebr \ u der Borntraeger, 1929.
34. A. G. Shtukenberg, A. Gujral, E. Rosseeva, X. Cui and B. Kahr, *CrystEngComm*, 2015, **17**, 8817--8824.
35. W. Cooper, N. Kenny, J. Edmonds, A. Nagel, F. Wudl and P. Coppens, *Journal of the Chemical Society D: Chemical Communications*, 1971, 889-890.
36. A. S. Batsanov, *Acta Crystallographica Section C: Crystal Structure Communications*, 2006, **62**, o501-o504.
37. D.-M. Smilgies and D. R. Blasini, *Journal of Applied Crystallography*, 2007, **40**, 716-718.
38. X. Cui, S. M. Nichols, O. Arteaga, J. Freudenthal, F. Paula, A. G. Shtukenberg and B. Kahr, *Journal of the American Chemical Society*, 2016, **138**, 12211-12218.
39. H.-M. Ye, J. H. Freudenthal, M. Tan, J. Yang and B. Kahr, *Macromolecules*, 2019, **52**, 8514-8520.
40. M. Tan, W. Jiang, A. T. Martin, A. G. Shtukenberg, M. D. McKee and B. Kahr, *Chemical Communications*, 2020, **56**, 7353-7356.
41. L. Helmbrecht, M. Tan, R. Röhrich, M. H. Bistervels, B. O. Kessels, A. F. Koenderink, B. Kahr and W. L. Noorduin, *Advanced Functional Materials*, 2020, **30**, 1908218.
42. R. Azzam, *Optics Letters*, 1978, **2**, 148-150.
43. O. Arteaga, M. Baldrís, J. Antó, A. Canillas, E. Pascual and E. Bertran, *Applied Optics*, 2014, **53**, 2236-2245.
44. X. Cui, A. L. Rohl, A. Shtukenberg and B. Kahr, *Journal of the American Chemical Society*, 2013, **135**, 3395--3398.
45. A. G. Shtukenberg, X. Cui, J. Freudenthal, E. Gunn, E. Camp and B. Kahr, *Journal of the American Chemical Society*, 2012, **134**, 6354-6364.
46. X. Cui, A. G. Shtukenberg, J. Freudenthal, S. Nichols and B. Kahr, *Journal of the American Chemical Society*, 2014, **136**, 5481-5490.
47. Y. Yang, Y. Zhang, C. T. Hu, M. Sun, S. Jeong, S. S. Lee, A. G. Shtukenberg and B. Kahr, *Chemistry of Materials*, 2022, DOI: 10.1021/acs.chemmater.1c04003.
48. Y. Yang, R. C. da Costa, M. J. Fuchter and A. J. Campbell, *Nature Photonics*, 2013, **7**, 634-638.
49. Y. Deng, M. Wang, Y. Zhuang, S. Liu, W. Huang and Q. Zhao, *Light: Science & Applications*, 2021, **10**.
50. J. R. Brandt, F. Salerno and M. J. Fuchter, *Nature Reviews Chemistry*, 2017, **1**, 0045.